

Modeling and sparsity-promoting separation of wind turbine noise in common-shot gathers

Yanglijiang Hu¹, Xiaokai Wang¹, Qinlong Hou¹, Dawei Liu², Xinmin Shang³, Meng Zhang³, and Wencho Chen¹

ABSTRACT

In land seismic acquisition, the quality of common-shot gathers is severely degraded by wind turbine noise (WTN) when wind turbines are operating continuously in survey areas. The high-amplitude WTN overlaps or even completely submerges the body and surface waves (signals). Through time-space and frequency analysis, three main features of the WTN are observed: (1) it is periodic with nearly constant frequencies over time, (2) it is coherent but exhibits different apparent velocities in space, and (3) it has relatively narrow bands with varying central frequencies. The first feature enables WTN to distort signals from shallow to deep, whereas the latter two features make traditional methods that separate noise and signals based on velocity and frequency differences less effective. To suppress the WTN, we first analyze its formation and propagation mechanism and then develop a WTN simulation model to validate the presented mechanism.

Based on our analysis of WTN and signals, we consider common-shot gathers as the linear superpositions of periodic WTN and relatively broadband signals (referred to as low-oscillatory signals). This additive mixture aligns with the feasibility premise of morphological component analysis (MCA). Finally, based on MCA theory, we develop a sparsity-promoting separation method to suppress WTN in common-shot gathers. To implement our separation method, we construct two dictionaries using the tunable Q -factor wavelet transform (TQWT) and the discrete cosine transform (DCT). TQWT and DCT can sparsely represent the oscillating waves (signals) and periodic waves (WTN), respectively. This work contributes to the existing knowledge of WTN separation by modeling the periodicity of WTN and the low-oscillatory behavior of a signal, rather than relying on velocity or frequency differences. Our method is tested on synthetic and field data, and both tests demonstrate its effectiveness in separating WTN and preserving signals.

INTRODUCTION

In land seismic acquisition, when wind turbines (Lyons et al., 2008; Walling et al., 2011) are operating continuously in the survey area, the quality of seismic data is severely degraded by wind turbine noise (WTN). The operation of wind turbines primarily involves the conversion of mechanical energy generated by the periodic rotations of blades and gears, as well as other components, into pressure energy that creates periodic impact pressure forces. The recording of seismic waves produced by these forces are called

WTN, which significantly degrades data quality and impedes the identification and extraction of waves used for seismic inversion.

Taking the three common-shot gathers contaminated by WTN shown in Figure 1, as an example we observe that various linear and hyperbolic WTN (the green arrows) are continuous in time and coherent in space. The coverage radius of WTN from a wind turbine is approximately 500 m, typically encompassing 25 neighboring traces, as indicated by the green box. Within the coverage of WTN, the body and surface waves from seismic sources referred to as signals (the red arrows in Figure 1), which are typically used for

Manuscript received by the Editor 14 January 2023; revised manuscript received 18 October 2023; published ahead of production 7 November 2023; published online 5 January 2024.

¹Xi'an Jiaotong University, School of Information and Communications Engineering, Xi'an, China. E-mail: 571635961@qq.com; xkwang@xjtu.edu.cn; houqinlong12@163.com; wencchen@xjtu.edu.cn (corresponding author).

²Xi'an Jiaotong University, School of Information and Communications Engineering, Xi'an, China and Purdue University, Department of Earth, Atmospheric, and Planetary Sciences, West Lafayette, Indiana, USA. E-mail: 409791715@qq.com.

³Sinopec Shengli Oilfield, Shengli Oilfield of SINOPEC, Geophysical Exploration Research Institute, Dongying, China. E-mail: shangxinmin.slyt@sinopec.com; zhangmeng886.slyt@sinopec.com.

© 2024 Society of Exploration Geophysicists. All rights reserved.

seismic imaging and inversion, are overlapped or even completely covered by WTN. Furthermore, WTN energy exhibits slow decay over time and strong coherence in space and time, resulting in the distortion of signals from shallow to deep. The WTN even completely submerges deep weak signals. In addition, the WTN in a trace exhibits multiple central frequencies, and different traces contain the WTN with distinct central frequencies. For instance, in Figure 2a–2d, we show the 84th, 150th, 357th, and 579th traces around the four arrows in Figure 1, and their corresponding time-frequency spectra are shown in Figure 2e–2h, respectively. In Figure 2f and 2g, the WTN (the red arrows) exhibits multiple narrow bands with strong amplitudes, particularly approximately 20 Hz as indicated by the black arrows, while displaying relatively weaker amplitudes for other central frequencies between 5 and 65 Hz. In Figure 2h, the WTN shows a strong narrow band at 30 Hz, as marked with a black arrow, and some harmonic frequencies are even observed at approximately 80 Hz, indicated by the red arrow. The WTN interferes with signals, ranging from 5 to 80 Hz, as shown in Figure 2e. The afore-

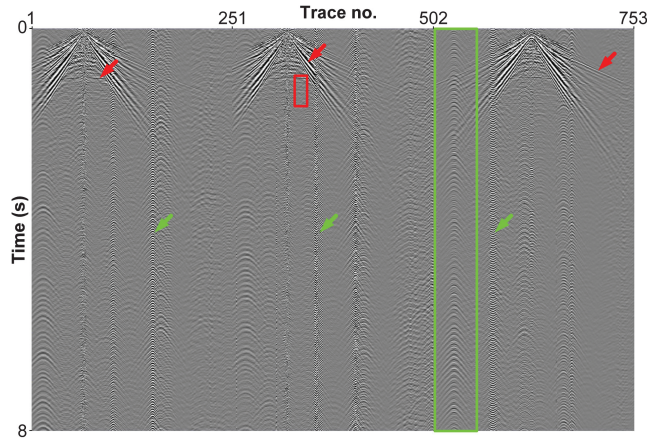


Figure 1. Three common-shot gathers consisting of WTN and signals. The WTN exhibits curve events (the two green arrows in the first and third gathers) and linear events (a green arrow in the second gather). The WTN mostly from one wind turbine is marked with the green box in the third gather. The signals are mainly reflections (a red arrow in the first gather and a red box in the second gather) and surface waves (two red arrows in the second and third gathers).

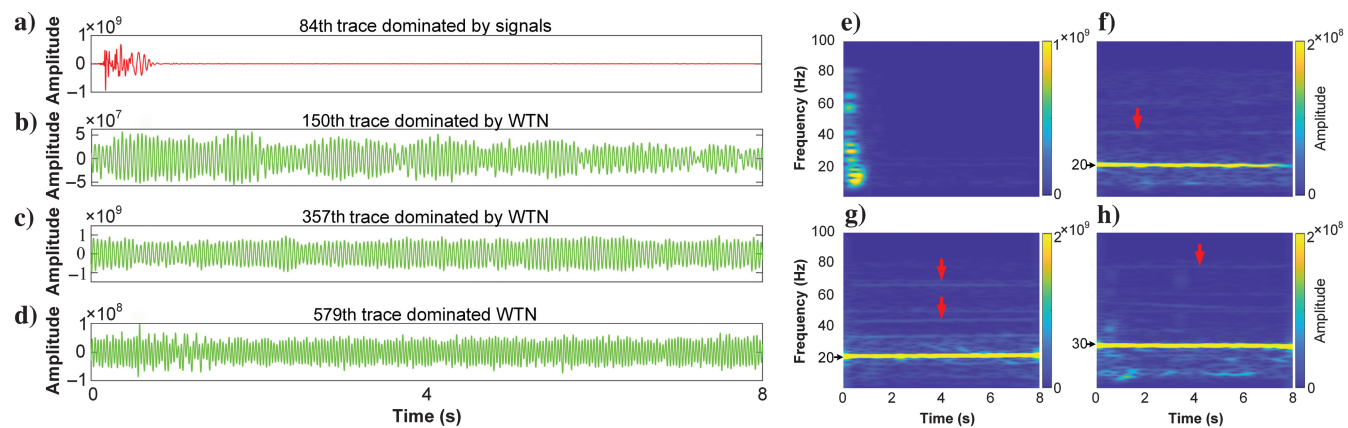


Figure 2. Four traces from Figure 1 and their time-frequency spectra: (a–d) 84th, 150th, 357th, and 579th traces extracted from Figure 1 and (e–h) their corresponding time-frequency spectra, respectively, where WTN energy exhibits narrow bands with different central frequencies (the four red arrows in [f–h]) and the strongest WTN energy is approximately 20 and 30 Hz as indicated by the black arrows.

mentioned analysis highlights the necessity and challenge of WTN separation. The diverse central frequencies of WTN are attributed to the different operating states of wind turbines, which are primarily influenced by time-varying wind speeds. Due to the diversity of WTN and its overlap with signals in the time and frequency domains, traditional filtering methods such as notch filtering and f - k filtering, which aim to separate noise based on frequency and velocity differences between noise and signals, are less effective.

An effective method for separating WTN is needed, but there has been limited direct research on WTN separation. However, due to the similarity between the narrow-band feature of WTN with a single central frequency and the narrow-band noise with fixed central frequencies (Li et al., 2021), such as drilling noise (Namuq and Reich, 2010) and pumping noise (Brandon et al., 1999; Wang et al., 2017), we have reviewed the following methods. Gao et al. (2011) propose an autocorrelation algorithm to estimate the narrow-band noise and subtract it using a cosine subtraction algorithm. Namuq et al. (2013) estimate the frequency range of the pumping noise in the continuous wavelet transform (CWT) domain and subtract it from the input data. Lin et al. (2018) use the Kalman filtering method to filter the pumping noise by predicting its frequencies and amplitudes. Qu et al. (2021) decompose the received signals into subcomponents using the empirical-mode decomposition and then reconstruct the pumping noise by combining some selected sub-components with adaptive weights. Although these methods have satisfactory performance in separating narrow-band noise with fixed central frequencies, they face challenges in separating WTN with various central frequencies. As shown in Figures 1 and 2, the WTN from different wind turbines at different locations exhibits multiple narrow bands with diverse central frequencies, making it difficult to identify its frequency ranges. WTN can be regarded as coherent noise in seismic data, similar to ground roll (Beresford-Smith and Rango, 1988; Liu et al., 2023) and harmonic noise (Lebedev and Beresnev, 2004). The coherent noise is often separated using sparse transforms such as the wavelet transform (Deighan and Watts, 1997; Yu and Garossino, 2005; Kulesh et al., 2007), the S-transform (Tao et al., 2020), and the curvelet transform (Liu et al., 2018, 2021a). The precondition for these methods is to find suitable transforms that can represent the waves of interest with as few coefficients as possible. In other words, the waves of interest are assumed to be sparsely represented by these

suitable transforms. However, it remains challenging to find a single transform that can sparsely represent complex seismic data, which are superpositions of the WTN and signals from complex surfaces and structures.

With the development of a sparse representation, the combination of multiple sparse transforms, known as dictionaries, has shown enhanced capabilities for sparse representations of complex seismic data compared with using a single transform. One notable approach that uses a combination of dictionaries is morphological component analysis (MCA) (Starck et al., 2004), which has been successful in decomposing complicated data into components with certain morphological features. MCA has two assumptions. First, it assumes that complex seismic data can be represented as a linear superposition of coherent noise and other waves with different morphological features. Second, each dictionary used in MCA is designed to sparsely represent a specific type of wave while being unable to sparsely represent other waves. In the case of WTN and signals that exhibit significant morphological differences, common-shot gathers can be considered as their linear superpositions, satisfying the first assumption of MCA.

The selection of appropriate dictionaries is a crucial step in fulfilling the second assumption of MCA. These dictionaries can be fixed transforms that are specifically designed to represent certain types of waves. Various studies have explored the use of different fixed sparse transforms in MCA, to separate specific wave components in seismic data. For instance, Yarham et al. (2006) use different curvelets to model the varying oscillation degrees of reflections and ground roll, enabling their separation through MCA. Wang et al. (2010) use the local discrete cosine transform (DCT) to sparsely represent ground roll, whereas the stationary symlet transform was used for representing reflections. In another MCA-based approach, Chen et al. (2017) use the tunable Q -factor wavelet transform (TQWT) with low and high Q -values to represent the low-oscillatory body waves and high-oscillatory ground roll separately. Chen et al. (2018) exploit the CWT and the DCT to achieve sparse representations of desired signals and distributed acoustic sensing coupling noise. Liu et al. (2022a) propose an MCA-based separation method that uses the chirplet transform and the CWT to model the different directions between harmonic noise and reflections, effectively suppressing harmonic noise while preserving reflections. In the tau- p domain, Liu et al. (2022b) use the 2D stationary wavelet transform to match the multiple reflection-refraction with the shape of points, whereas the shearlet transform was used to represent the other waves with the shape of curves. These studies demonstrate the versatility and effectiveness of using different fixed sparse transforms for the MCA-based separation. Apart from fixed transforms, the use of adaptive transforms in coherent noise attenuation has also been explored in previous studies (Olshausen and Field, 1996; Aharon et al., 2006; Rubinstein et al., 2010, 2013; Liu et al., 2019, 2021b; Guo et al., 2021). Adaptive transforms offer flexibility by allowing updates based on local data. However, in the context of MCA applications, fixed transforms offer simplicity and can be directly applied based on a professional understanding of the target waves and existing knowledge of transforms. Considering our research on WTN and the existing work on fixed transforms, our approach centers around using fixed transforms to construct dictionaries for modeling the morphological features of WTN and signals. Based on MCA theory and the dictionaries that we construct, this paper proposes a sparsity-promoting separation method for effectively separating WTN from common-shot gathers.

Our work can be summarized into three main contributions. (1) We present the formation and propagation mechanism of WTN and propose a WTN simulation model based on the presented mechanism. By studying the formation and propagation mechanism of WTN, we gain insights into the periodic and almost constant frequency behavior of WTN in seismic gathers. To validate the rationality of the presented mechanism, we simulate WTN based on the proposed WTN simulation model and then compare the simulated WTN with the actual WTN. (2) We develop a strategy for constructing dictionaries using 1D DCT and TQWT to sparsely represent WTN and signals. The presented formation and propagation mechanism of WTN show that WTN in gathers is periodic and has almost constant frequencies in time. In addition, signals shown in Figure 2e have relatively broadband and low-oscillation behavior. Based on the observed morphological features of WTN and signals, we assume that each common-shot gather is a linear superposition of periodic WTN and low-oscillatory signals. Accordingly, we construct dictionaries using the TQWT with a low Q -value for representing low-oscillatory signals and the 1D DCT for representing periodic WTN. (3) We propose a separation method that combines MCA with the constructed dictionaries to separate WTN trace by trace. Our method is applied to synthetic and field data, and its effectiveness is demonstrated by comparing the separated results with those obtained using a high-energy noise attenuation method, which is commonly used in the industry (Yu and Garossino, 2005). Overall, our research contributes to the understanding of WTN, provides a practical approach for their separation using MCA and constructed dictionaries, and demonstrates the superiority of our method through comparisons with existing noise attenuation techniques.

The rest of the paper is divided into five parts. The first part describes the analysis and modeling of WTN. The second part introduces the separation method based on MCA. The third part depicts our dictionary construction strategy, including the introduction of the 1D DCT and the TQWT as well as the analysis of the utility of the constructed dictionaries. The fourth part illustrates the synthetic data and field data examples. Finally, in the fifth part, we present the conclusions.

THE ANALYSIS AND MODEL OF WTN

Figure 3a shows one simple wind turbine structure, and Figure 3b shows the typical drive train configuration of the wind turbine (Oyague, 2009; Dong et al., 2012). In Figure 3b, three blades are attached to the hub. The rotating speed of the blades (usually between 19 r/min [0.3167 r/s] and 35 r/min [0.5833 r/s]) is relatively low and insufficient to generate power directly. However, the gearbox shown in Figure 3b can increase the rotating speed of the shaft with a typical gear ratio of 50. As a result, the rotating speeds of the high-speed shaft are typically between 15.8 and 29.2 r/s. The periodic motions of the rotating blades, gearbox, high-speed shaft, and other operating components generate periodic impact pressure forces that stimulate seismic waves near the ground surface. If we use $\mathbf{w}(t)$ to denote the seismic response near the wind turbine generating one cycle impact pressure force, the entire seismic response near the wind turbine can be modeled as

$$\mathbf{s}(t) = A \sum_{n=-\infty}^{+\infty} \mathbf{w}(t - n\tau), \quad (1)$$

where τ is the period of cycle impact pressure force and A is their amplitude. The values of τ and A remain almost constant within one shot time. If there are M different types of cycle impact pressure forces, the entire seismic response near the wind turbine can be modeled as

$$\mathbf{s}(t) = \sum_{m=1}^M A_m \sum_{n=-\infty}^{+\infty} \mathbf{w}_m(t - n\tau_m), \quad (2)$$

where τ_m and A_m represent the period and the amplitude of the m th type of cycle impact pressure force, respectively.

The estimated apparent velocities of WTN shown in Figure 1 range between 600 and 1300 m/s, which differ from the velocities of reflections but align with those of some surface waves. These findings suggest that WTN directly reaches the receiver station along the surface, as shown in Figure 3c. The dashed red lines

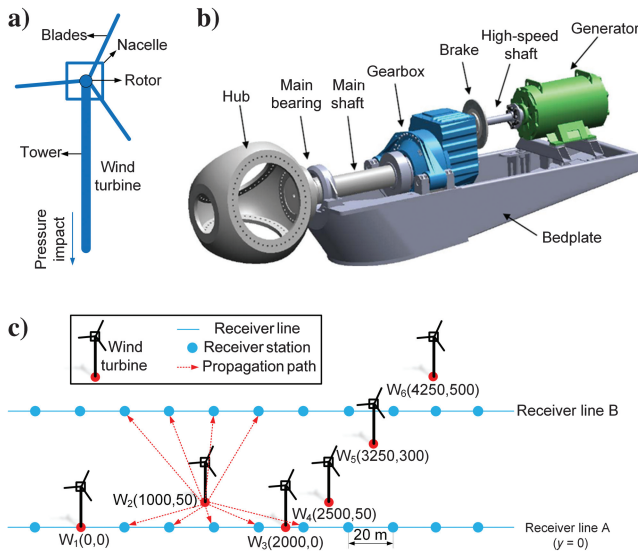


Figure 3. Demonstration of WTN propagation and formation mechanism: (a) wind turbine structure, (b) drive train configuration of the wind turbine, and (c) schematic diagram of a 3D seismic observation system.

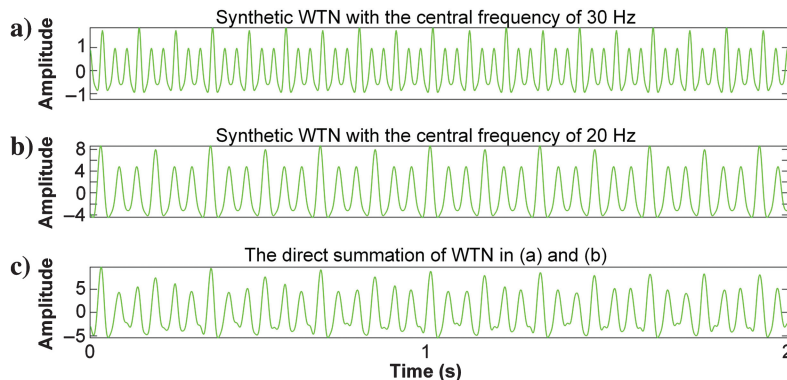


Figure 4. Synthetic WTN traces from the proposed simulation model. (a–c) Three synthetic traces and (d–f) their corresponding time-frequency spectra, respectively.

in Figure 3c show some wave propagation paths from the wind turbine W_2 to some nearby receivers.

We suppose that the apparent velocity of WTN is v . If one wind turbine's position is represented by (x_0, y_0) , then the WTN generated by this wind turbine can be recorded by the receiver with position (x_r, y_r) :

$$\begin{aligned} \mathbf{s}(x_0, y_0; x_r, y_r, t) &= \frac{1}{\sqrt{d}} \mathbf{s}\left(t - \frac{d}{v}\right) \\ &= \frac{1}{\sqrt{d}} \sum_{m=1}^M A_m \sum_{n=-\infty}^{+\infty} \mathbf{w}_m\left(t - n\tau_m - \frac{d}{v}\right), \end{aligned} \quad (3)$$

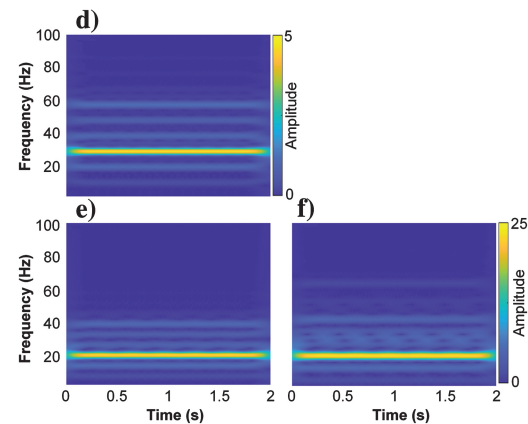
where

$$d = \sqrt{(x_0 - x_r)^2 + (y_0 - y_r)^2}. \quad (4)$$

If there are multiple wind turbines in one survey, the recorded WTN by one receiver can be obtained by the linear superposition of the WTN generated by multiple turbines.

Usually, the high-speed shaft's rotation is a main WTN source. The typical high-speed shaft's rotating speed is between 15.8 and 29.2 r/s, leading to seismic responses with the central frequencies between 15.8 and 29.2 Hz. Accordingly, the central frequencies of the strongest WTN should be between 15.8 and 29.2 Hz. The field WTN in the time-frequency domain, as shown in Figure 2f–2h, has dominant energy near 20 and 30 Hz, which indicates that the high-speed shaft's rotation is a main WTN source.

Based on the main energy of approximately 30 and 20 Hz of typical WTN in the field data, we initially define two types of periodic impact pressure forces generated by each wind turbine. The periods, τ_1 and τ_2 , are set to 0.033 and 0.05 s, respectively. In addition, to make the features (e.g., waveform and frequency distribution) of the synthetic WTN similar to that of the field WTN shown in Figure 2b and 2d, we set $\mathbf{w}_1(t)$ to a 30 Hz Ricker wavelet and $\mathbf{w}_2(t)$ to a 20 Hz Ricker wavelet. The synthetic traces corresponding to these parameters are shown in Figure 4a and 4b, respectively, each consisting of 1000 samples. Figure 4c shows their direct summation. The time-frequency spectra of Figure 4a–4c are shown in Figure 4d–4f, respectively. Similar to the observations in Figure 2f–2h, the main



energy of WTN in Figure 4d–4f is approximately 20, 20, and 30 Hz. In addition, there are several bands with relatively weaker energy with their central frequencies shifting between 5 and 65 Hz. However, a noticeable difference is the presence of more visible sidelobes near 30 and 20 Hz in Figure 4d and 4e compared with Figure 2h and 2f. This inconsistency arises because field data contain more diverse waves than synthetic data. Some sidelobes near 20 or 30 Hz in Figure 2f and 2h are invisible, but their amplitudes are much weaker than those of other bands in the frequency domain. These observations serve to validate the rationality of the presented time-frequency model of WTN.

To synthesize the WTN in one 2D data set, we also set the periods, τ_1 and τ_2 , to 0.033 and 0.05 s, respectively. In addition, we set $\mathbf{w}_1(t)$ to a 30 Hz Ricker wavelet and $\mathbf{w}_2(t)$ to a 20 Hz Ricker wavelet. The amplitude of $\mathbf{w}_1(t)$ is set to two, whereas the amplitude of $\mathbf{w}_2(t)$ is set to 10. Using the observation system shown in Figure 3c, we simulate the WTN generated by six wind turbines W_1, W_2, \dots, W_6 and propagating to the receiver line A. Figure 5 shows the direct summation of the simulated WTN, comprising 240 traces and 1000 samples per trace. The sampling interval between samples is 0.002 s. The distance between two adjacent traces is 20 m. In Figure 5, the coverage radius of the WTN induced by each wind turbine is 500 m. The WTN generated by the wind turbines on receiver line A (W_1 and W_3) appears as linear events, whereas the WTN generated from other turbines (W_2, W_4, W_5 , and W_6) appears as hyperbolic events. This observation is consistent with the characteristics of WTN observed in the common-shot gather, as shown in Figure 1.

SEPARATION METHOD BASED ON MCA

The MCA is a general model used for separating a complex data set \mathbf{s} into its constituent components $\mathbf{s}_1, \mathbf{s}_2, \dots, \mathbf{s}_n$, each with different morphological features. In the context of MCA, a complex data set is considered to be a linear superposition of n components:

$$\mathbf{s} = \sum_{i=1}^n \mathbf{s}_i. \quad (5)$$

Each component $\mathbf{s}_i, i \in \{1, \dots, n\}$ is assumed to be reconstructed by a sparse representation \mathbf{x}_i of a dictionary \mathbf{D}_i , that is, $\mathbf{s}_i = \mathbf{D}_i \mathbf{x}_i$. Based on these assumptions, the separation problem is

$$\{\mathbf{x}_i^{\text{opt}}\}_{i=1}^n = \arg \min_{\{\mathbf{x}_i\}_{i=1}^n} \sum_{i=1}^n \|\mathbf{x}_i\|_1 + \lambda \left\| \mathbf{s} - \sum_{i=1}^n \mathbf{D}_i \mathbf{x}_i \right\|_2^2, \quad (6)$$

where $\mathbf{x}_i^{\text{opt}}$ is the sparse representation of a component to be separated and λ is a Lagrange multiplier. Here, $\mathbf{s}_i^{\text{opt}} = \mathbf{D}_i \mathbf{x}_i^{\text{opt}}$ is the separated component. The problem in equation 6 is usually solved by the block coordinate relaxation algorithm (Bruce et al., 1998).

In this paper, a seismic trace $\mathbf{s} \in \mathbf{R}^{L_s}$ having L_s samples consists of the signals \mathbf{s}_1 and the WTN \mathbf{s}_2 , which is expressed as

$$\mathbf{s} = \mathbf{s}_1 + \mathbf{s}_2. \quad (7)$$

Based on MCA, sparse representations $\mathbf{x}_1^{\text{opt}}$ and $\mathbf{x}_2^{\text{opt}}$ of \mathbf{s}_1 and \mathbf{s}_2 , respectively, are computed by solving the following problem:

$$\{\mathbf{x}_1^{\text{opt}}, \mathbf{x}_2^{\text{opt}}\} = \arg \min_{\{\mathbf{x}_1, \mathbf{x}_2\}} \|\mathbf{x}_1\|_1 + \|\mathbf{x}_2\|_1 + \lambda \left\| \mathbf{s} - \sum_{i=1}^2 \mathbf{D}_i \mathbf{x}_i \right\|_2^2, \quad (8)$$

where \mathbf{D}_1 and \mathbf{D}_2 are the preconstructed dictionaries for \mathbf{s}_1 and \mathbf{s}_2 , respectively, and $\mathbf{s}_1^{\text{opt}} = \mathbf{D}_1 \mathbf{x}_1^{\text{opt}}$ and $\mathbf{s}_2^{\text{opt}} = \mathbf{D}_2 \mathbf{x}_2^{\text{opt}}$ are the separated WTN and signals, respectively. The MCA used for WTN separation is effective on the premise that the dictionary \mathbf{D}_1 in equation 8 sparsely represents the signals and is highly ineffective in representing the WTN, whereas the dictionary \mathbf{D}_2 in equation 8 sparsely represents the WTN and is highly ineffective in representing the signals.

If the morphological features of the waveform atom of one transform match that of a specific wave, the transform exhibits a strong sparse representation capability for that wave. As shown in Figures 1, 2, and 4, WTN exhibits periodicity in the time domain and relatively narrow frequency bands, whereas signals display low oscillation in the time domain and wider frequency bandwidths. These morphological differences serve as a guide for selecting appropriate dictionaries. In this regard, the 1D DCT is well-suited for sparsely representing periodic waves, whereas the TQWT with a small Q -value is effective in representing low-oscillation waves. Therefore, we anticipate that the 1D DCT and TQWT serve as representative dictionaries for WTN and signals, respectively.

DICTIONARY CONSTRUCTION STRATEGY

The first two parts of this section, respectively, introduce the TQWT and the 1D DCT, which we have selected to meet the requirements of the MCA-based WTN separation. Subsequently, we provide a brief explanation for why we have chosen TQWT and 1D DCT to represent signals and WTN, respectively. In the third part, we conduct a detailed analysis to assess the utility of chosen dictionaries.

Tunable Q -factor wavelet transform

The TQWT uses filter banks in the frequency domain to represent waveforms. It consists of a high-pass filter $G_j(f)$ and a low-pass filter $H_j(f)$ at a wavelet-level $j \in \{1, 2, \dots, J\}$ where J is the

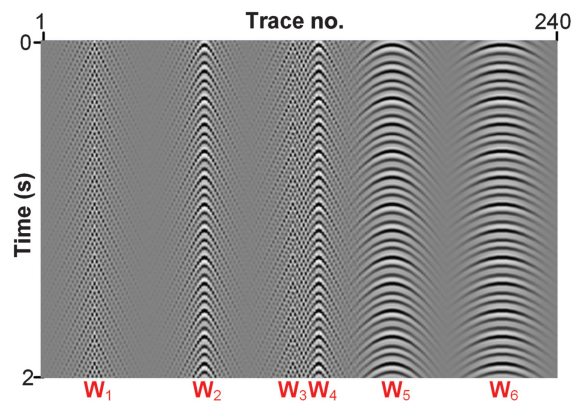


Figure 5. Simulated WTN generated by wind turbines W_1, W_2, \dots, W_6 and received by the receiver line A in Figure 3c, respectively, and the name of the turbine corresponding to the WTN is given in red at the bottom of the figure.

number of the filtering bank (Selesnick, 2011a). The low-pass output of each filter bank is used as the input to the successive filter bank. For an input signal $s(t)$ with a sampling rate of f_s , the main flow of a TQWT is shown in Figure 6, where $j \in \{1, \dots, J\}$, α_j is a low-passed signal, β_j is a high-passed signal, and $G_j^-(f)$ and $H_j^-(f)$ are the reconstruction functions. Here, $G_j(f)$ and $H_j(f)$ depend on two scaling parameters $b_1, b_2 \in (0, 1]$ that are

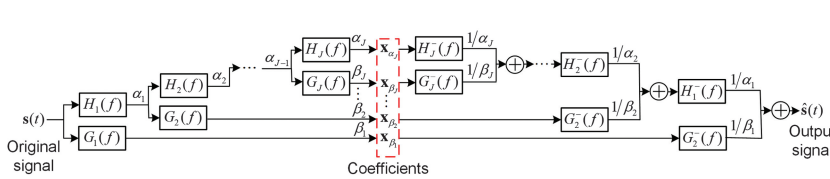


Figure 6. The main flow of the decomposition and reconstruction of the TQWT.

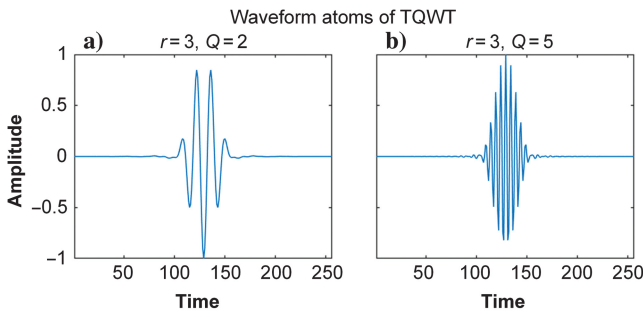


Figure 7. Two TQWT atoms: (a) the atom with $r = 3$ and $Q = 2$ and (b) the atom with $r = 3$ and $Q = 5$.

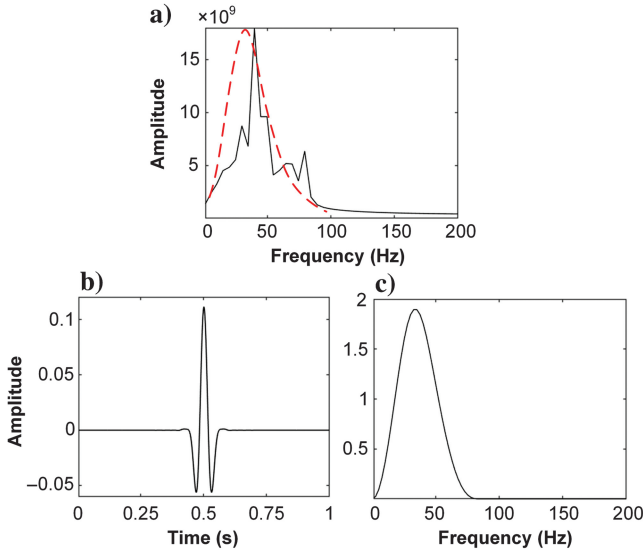


Figure 8. Comparison between the signal-dominated data segment and the waveform of the constructed TQWT. (a) Average amplitude spectra of the data of 330th to 340th traces and 0.48–0.70 s in Figure 1 and the dotted red curve is its fitted energy envelope, (b) waveform of the TQWT ($Q = 1$), and (c) frequency spectrum of the waveform atom in (b).

$$b_1 = 2/(Q + 1), \quad b_2 = 1 - b_1/r, \quad (9)$$

where Q is the Q -value and r is the redundancy factor. The redundancy factor is defined as the ratio of the total number of coefficients representing a wave and the original number of sampling points of the wave. Here, Q plays a significant role as it affects the oscillation degree of the TQWT atom waveform. The Q -value is expressed as

$$Q = \frac{f_0}{\text{BW}}, \quad (10)$$

where f_0 is the central frequency of the waveform atom and BW is its bandwidth. Based on equations 9 and 10, the frequency responses of $H_0(f)$ and $G_0(f)$ are expressed as

$$H_0(f) = \begin{cases} 1 & |f| \leq (1 - b_1)\pi \\ \theta\left(\frac{f+(b_1-1)\pi}{b_2+b_1-1}\right) & (1 - b_1)\pi < |f| < b_2\pi, \\ 0 & b_2\pi \leq |f| \leq \pi \end{cases}$$

$$G_0(f) = \begin{cases} 0 & |f| \leq (1 - b_1)\pi \\ \theta\left(\frac{b_2\pi-f}{b_2+b_1-1}\right) & (1 - b_1)\pi < |f| < b_2\pi, \\ 1 & b_2\pi \leq |f| \leq \pi \end{cases}, \quad (11)$$

where $\theta(f) = 0.5(1 + \cos f)\sqrt{2 - \cos f}, |f| \leq \pi$. Here, $H_{j>0}(f)$ and $G_{j>0}(f)$ are calculated based on $H_0(f)$ and $G_0(f)$ (Selesnick, 2011b). By increasing the value of Q , the waveform atoms of the TQWT become more oscillatory. The wavelet-level j does not significantly affect the overall shape of the waveform of the TQWT in the frequency domain. Assuming a redundancy factor of 3 ($r = 3$), Figure 7 shows two TQWT atoms with Q -values of two and five, respectively, showcasing different degrees of oscillation. From the preceding discussion, it is evident that adjustable Q -values allow TQWT to flexibly match the oscillation behaviors of waves, and selecting an appropriate Q -value is crucial for constructing a TQWT dictionary for signals with low oscillation.

As described by Selesnick (2011a), r is recommended to be three or greater to align the TQWT atoms with the fast decay of seismic wavelets. Hence, we only focus on estimating the Q -value. We calculate the Q -value based on the central frequency and bandwidth of the local data segments occupied by signal energy in given data, rather than selecting a Q -value empirically. For illustration purposes, field data are used in this section. Although pure signals do not exist in reality, data fragments that are dominated by signal energy can be approximately treated as pure signals. Thus, a data fragment in the red box in Figure 1, spanning from the 330th to 340th traces and from 0.48 to 0.70 s, which is dominated by signal energy, is taken as a reference for estimating the Q -value of TQWT. Figure 8a shows the average amplitude spectrum of this data fragment. Its central frequency is approximately 35 Hz, and its bandwidth is approximately 30 Hz, resulting in a ratio of approximately one. In comparison, Figure 8b and 8c, respectively, shows the waveform atom of the TQWT with $Q = 1$ and its frequency spectrum. The spectrum in Figure 8c exhibits a central frequency of approximately

30 Hz and a bandwidth of approximately 35 Hz, which closely resembles the spectrum shown in Figure 8a. This similarity indicates that the oscillation of the waveform of the TQWT with $Q = 1$ matches the oscillation of the data segment dominated by signal energy. Therefore, the TQWT with $Q = 1$ is used as the dictionary for representing signals.

1D discrete cosine transform

The 1D DCT is derived from the discrete Fourier transform. It works with fixed parameters. The sparse presentation of the 1D DCT of a discrete waveform $\mathbf{s}[\cdot]$ with the length of n is

$$\mathbf{x}_{\text{DCT}}[k] = A_k \sum_{u=0}^{n-1} \mathbf{s}[u] \cos \frac{(0.5+u)k\pi}{n}, \quad k = 0, \dots, n-1,$$

$$A_k = \begin{cases} \sqrt{\frac{1}{n}} & k = 0, \\ \sqrt{\frac{2}{n}} & k > 0. \end{cases} \quad (12)$$

The recovered waveform $\hat{\mathbf{s}}_{\text{DCT}}[\cdot]$ is

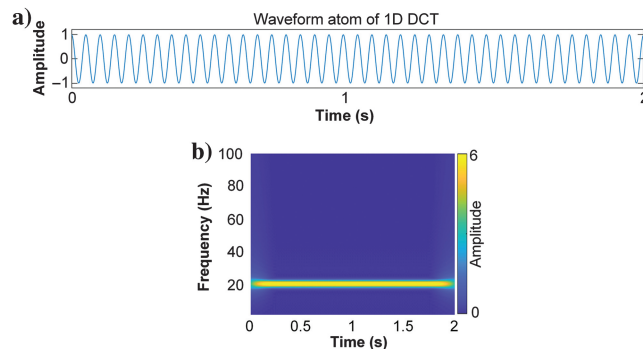


Figure 9. (a) The waveform of an atom in the 1D DCT and (b) the time-frequency spectrum of (a).



Figure 10. A trace of synthetic signal.

$$\hat{\mathbf{s}}_{\text{DCT}}[u] = \sum_{k=0}^{n-1} A_k \mathbf{x}_{\text{DCT}}[k] \cos \frac{(0.5+u)k\pi}{n}, \quad u = 0, \dots, n-1. \quad (13)$$

Figure 9a and 9b shows the waveform of an atom in 1D DCT and its corresponding time-frequency spectrum, respectively. In Figure 9a, the atom exhibits temporal continuity and periodicity. In Figure 9b, it appears as a relatively narrow band. These findings suggest that the periodicity of a 1D DCT atom matches the periodicity of WTN. Thus, we choose the 1D DCT as the dictionary for representing WTN.

Analysis of the feasibility of the chosen dictionaries

As described in the “Separation method based on MCA” section, a prerequisite of the MCA-based WTN separation is to construct two dictionaries. One dictionary sparsely represents signals and does not sparsely represent WTN, whereas the other sparsely represents WTN and does not sparsely represent signals. To assess the feasibility of the chosen dictionaries, we use a sparsity function (Hoyer, 2004) to quantify the sparsity of various waves represented

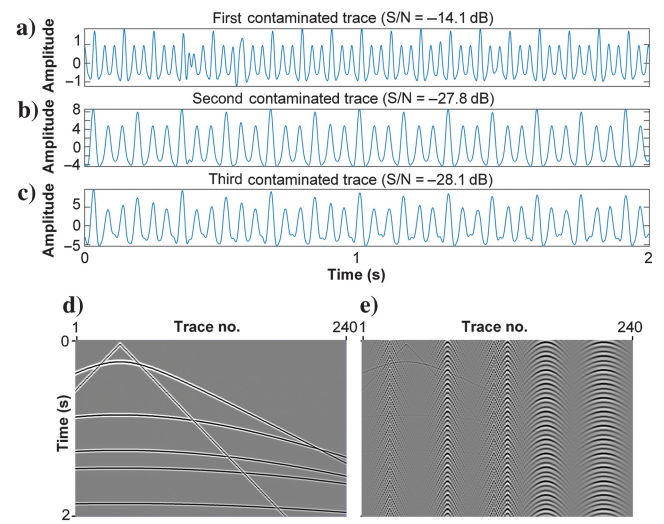


Figure 11. The 1D and 2D synthetic data examples. (a–c) Three contaminated traces obtained by adding the synthesized signals (Figure 10) to WTN shown in Figure 4a–4c, respectively; (d) synthetic signal; and (e) 2D contaminated data obtained by adding the synthetic signal (d) to the synthetic WTN shown in Figure 5.

Table 1. Comparison of the sparsity of four different dictionaries in representing four typical traces, which are dominated by the field signal (Figure 2a), synthetic signal (Figure 10), field WTN (Figure 2b), and synthetic WTN (Figure 4c), respectively.

Dictionaries	The main waveform in a trace			
	Synthetic signal (Figure 10)	Synthetic WTN (Figure 4c)	Field signal (Figure 2a)	Field WTN (Figure 2b)
TQWT (with $Q = 1$)	0.7856	0.3880	0.8124	0.3832
1D DCT	0.6527	0.8707	0.6052	0.8753
CWT (Morlet)	0.7564	0.5896	0.8534	0.6667
SWT (biorthogonal)	0.8169	0.5659	0.8766	0.6557

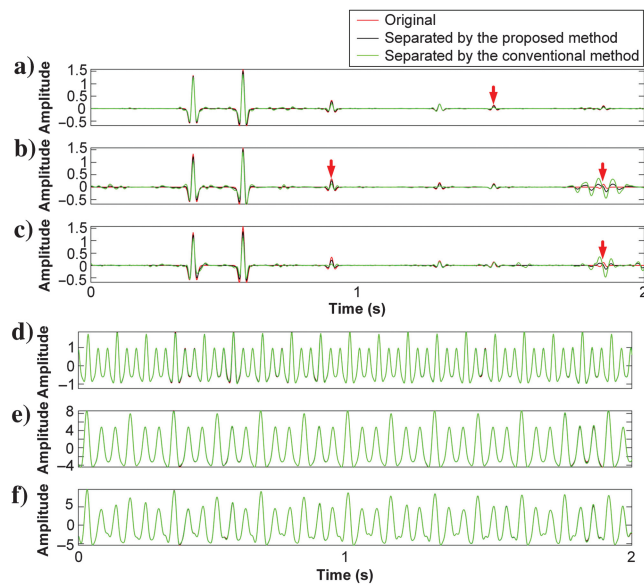


Figure 12. A comparison of separation results for three contaminated traces shown in Figure 11a–11c. (a–c) Original synthetic signals (the red curves), the separated synthetic signals obtained by applying the proposed method (the black curves), and the conventional method (the green curves), respectively, and (d–f) the original synthetic WTN (the red curves), the separated synthetic WTN obtained by applying the proposed method (the black curves), and the conventional method (the green curves), respectively.

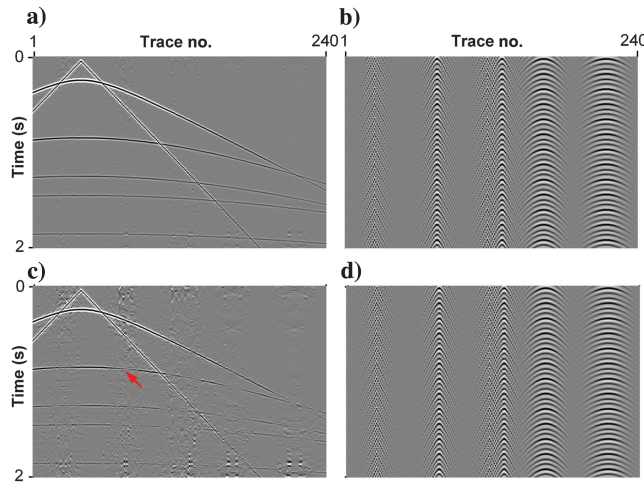


Figure 13. A comparison of separation results for the contaminated 2D data shown in Figure 11e. (a and b) Separated signals and WTN obtained by applying the proposed method and (c and d) separated signals and WTN obtained by applying the conventional method, and a region with the signal damage (red arrow in [c]).

by four different transforms: TQWT with $Q = 1$ (selected for signals), 1D DCT (selected for WTN), CWT (Morlet), and the stationary wavelet transform with the biorthogonal wavelet (SWT [biorthogonal]). The sparsity is measured based on the total number of coefficients, denoted as L , in a representation matrix \mathbf{x} obtained by applying a transform to input data. This sparseness function is

$$\text{sparseness}(\mathbf{x}) = \frac{\sqrt{L} - \|\mathbf{x}\|_1/\|\mathbf{x}\|_2}{\sqrt{L} - 1}. \quad (14)$$

Here, $\text{sparseness}(\mathbf{x}) = 1$ if and only if \mathbf{x} has only one nonzero component equal to one, that is, the closer to 1 the value of $\text{sparseness}(\mathbf{x})$ is, sparser the \mathbf{x} is.

To compare the sparsity of signals and WTN represented by the four transforms, we analyze four traces dominated by field signal (Figure 2a), synthetic signal (Figure 10), field WTN (Figure 2b), and synthetic WTN (Figure 4c). The sparsity values are calculated in formula 14 using these traces and four transforms, which are presented in Table 1. From Table 1, we observe that the sparsity values of the two signal-dominated traces represented by TQWT (0.7856 and 0.8124) are much closer to one compared with the sparsity values of the two WTN-dominated traces represented by the TQWT (0.3880 and 0.3832). Similarly, the sparsity values of the two WTN-dominated traces represented by the 1D DCT (0.8707 and 0.8753) are much closer to one than the sparsity values of the two signal-dominated traces represented by the 1D DCT (0.6527 and 0.6052).

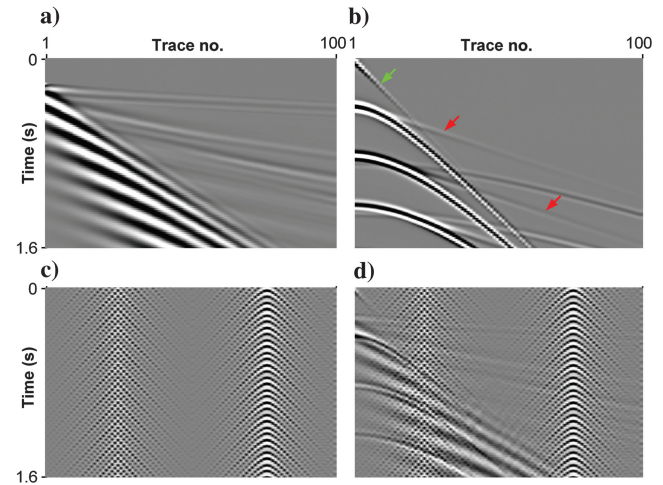


Figure 14. Second synthetic data example: (a) synthetic surface waves, (b) synthetic direct waves (green arrow) and reflections and refractions (two red arrows), (c) synthetic WTN, and (d) the contaminated data consisting of waves shown in (a–c).

Table 2. The S/N comparison of the separated signals for three typical traces (Figure 11a–11c) and 2D synthetic data (Figure 11e).

		Traces (Figure 11a–11c)			
		First	Second	Third	2D data (Figure 11e)
Contaminated (dB)		−14.1	−27.8	−28.1	−23.5
Separated (dB)	The proposed method	20.1	13.5	13.3	19.9
	The conventional method	13.1	5.0	5.4	11.3

In addition, in Table 1, the sparsity differences between the synthetic signal- and noise-dominated traces represented by the CWT (Morlet) and the SWT (biorthogonal) (0.1664 and 0.2510), respectively, are smaller than the sparsity difference between those represented by the TQWT (0.3976). Moreover, the sparsity differences between the field signal- and noise-dominated traces represented by the CWT (Morlet) and the SWT (biorthogonal) (0.1867 and 0.2209), respectively, are also smaller than the sparsity difference between those represented by the TQWT (0.4292). These results indicate that the TQWT exhibits a clearer distinction in representing signals and WTN in terms of sparsity than the CWT (Morlet) and the SWT (biorthogonal). In summary, the comparisons in Table 1 demonstrate two important facts: (1) the 1D DCT represents

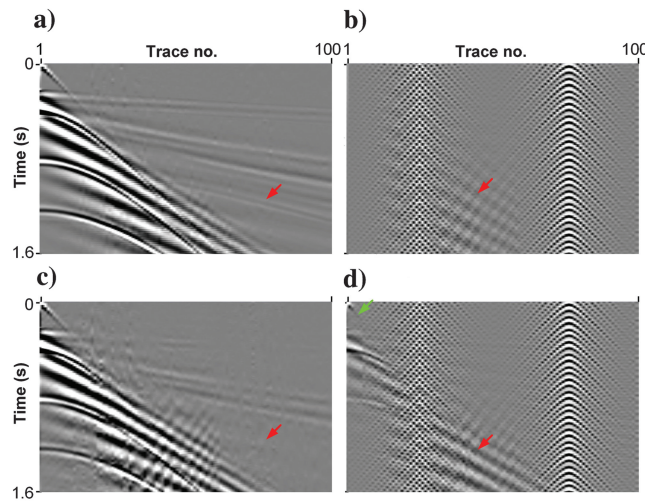


Figure 15. A comparison of separation results for the second synthetic data example shown in Figure 14d (some surface waves are marked with red arrows in [a–d] and direct waves are marked with a green arrow in [d]). (a and b) Separated signals and WTN obtained by applying the proposed method and (c and d) separated signals and WTN obtained by applying the conventional method.

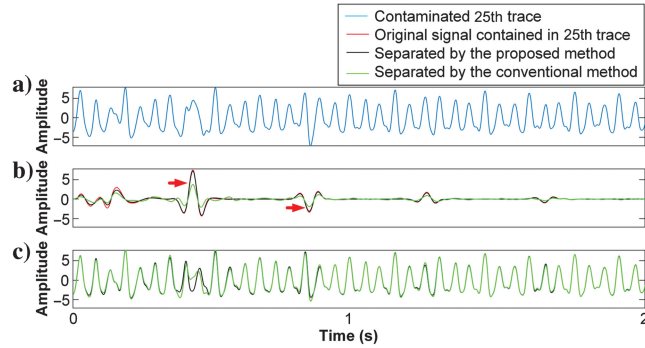


Figure 16. Comparison of the 25th contaminated trace in the second synthetic data example. (a) The 25th contaminated trace; (b) original signal contained in the contaminated trace (red curve), the separated signal obtained by applying the proposed method (black curve), and the conventional method (green curve), not some areas with obvious amplitude differences are marked with the red arrows; and (c) original WTN contained in the contaminated trace (red curve), the separated WTN obtained by applying the proposed method (black curve), and the conventional method (green curve).

WTN-dominated traces much more sparsely than the signal-dominated traces it represents and (2) the TQWT with $Q = 1$ represents signal-dominated traces much more sparsely than the WTN-dominated traces it represents.

The facts presented here provide evidence that the constructed TQWT and 1D DCT dictionaries fulfill the prerequisite of the MCA-based WTN separation, as mentioned in the initial sentences of this section.

EXAMPLE

This section aims to demonstrate the effectiveness of the proposed method, which uses MCA with the TQWT ($Q = 1$) and the 1D DCT, on synthetic data and common-shot gathers. The high-energy noise attenuation method in the stationary biorthogonal-wave-

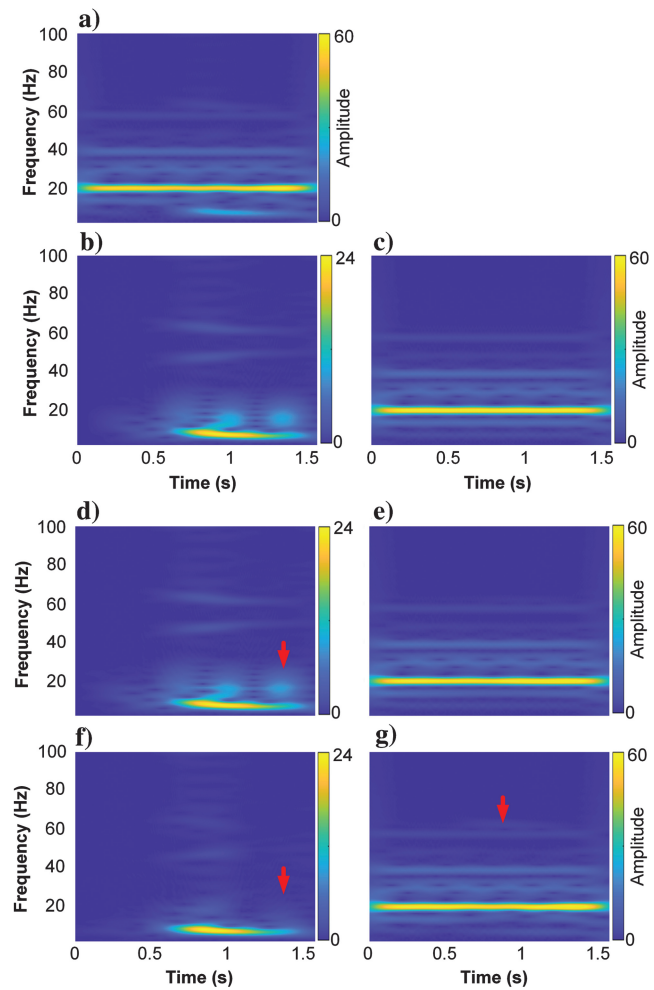


Figure 17. Comparison of time-frequency spectra of the 25th contaminated trace in the second synthetic data example (some areas with obvious amplitude differences are marked with the red arrows in [d, f and g]). (a) Time-frequency spectrum of the contaminated trace; (b and c) time-frequency spectra of the signal and WTN contained in the contaminated trace, respectively; (d and e) time-frequency spectra of the separated signal and WTN obtained by applying the proposed method, respectively; and (f and g) time-frequency spectra of the separated signal and WTN obtained by applying the conventional method, respectively.

let transform domain (Yu and Garossino, 2005) is selected as the conventional method for comparison.

First synthetic data application

In this part, we evaluate the performance of the proposed method using synthetic traces and common-shot gathers. First, we add the signals shown in Figure 10 to the WTN shown in Figure 4a–4c, resulting in three contaminated traces displayed in Figure 11a–11c. In addition, Figure 11d shows six synthetic signal events synthesized using the Ricker wavelet with a central frequency of 30 Hz. The contaminated data shown in Figure 11e are a summation of the synthetic WTN from Figure 5 and the synthetic signals from Figure 11d.

The separated results for three synthetic traces (Figure 11a–11c) are shown in Figure 12. All of the separated results exhibit the signals and WTN that closely resemble the original signals and WTN (the red curves). However, compared with the separated signals and WTN obtained from the conventional method (the green curves), the separated signals and WTN obtained from the proposed method (the black curves) are closer to the original signals and WTN. Figure 13a and 13b, respectively, shows the separated signals and WTN obtained by applying the proposed method to the synthetic gather (Figure 11e). Figure 13c and 13d, respectively, shows the separated signals and WTN obtained by applying the conventional method to

the same synthetic gather. Figure 13a exhibits clearer signals than Figure 13c where some signal damages are indicated by a red arrow. The signal-to-noise ratios (S/Ns) of the contaminated data and separated signals are provided in Table 2. Although the S/Ns of the separated results are all higher than those of the contaminated data, the S/Ns of the separated signals from the proposed method are 7, 8.5, 7.9, and 8.6 dB higher than those of the separated signals from the conventional method, respectively. These results demonstrate that the proposed method is more effective in separating synthetic WTN and preserving synthetic signals compared with the conventional method.

Second synthetic data application

In this part, we use two modeling techniques to generate the seismic components for our analysis. First, we use the ground-roll modeling method described by Chen et al. (2017) to generate the ground roll shown in Figure 14a. The ground roll is obtained using the Fuchs-Muller wavelet with a dominant frequency of 8 Hz. Second, we apply the reflection-refraction modeling method described by Hu et al. (2022) to generate refractions (indicated by the red arrows) and direct waves (indicated by a green arrow) shown in Figure 14b. These synthetic components have a central frequency of 30 Hz and are obtained from a four-layer geologic model with a 30 Hz Ricker

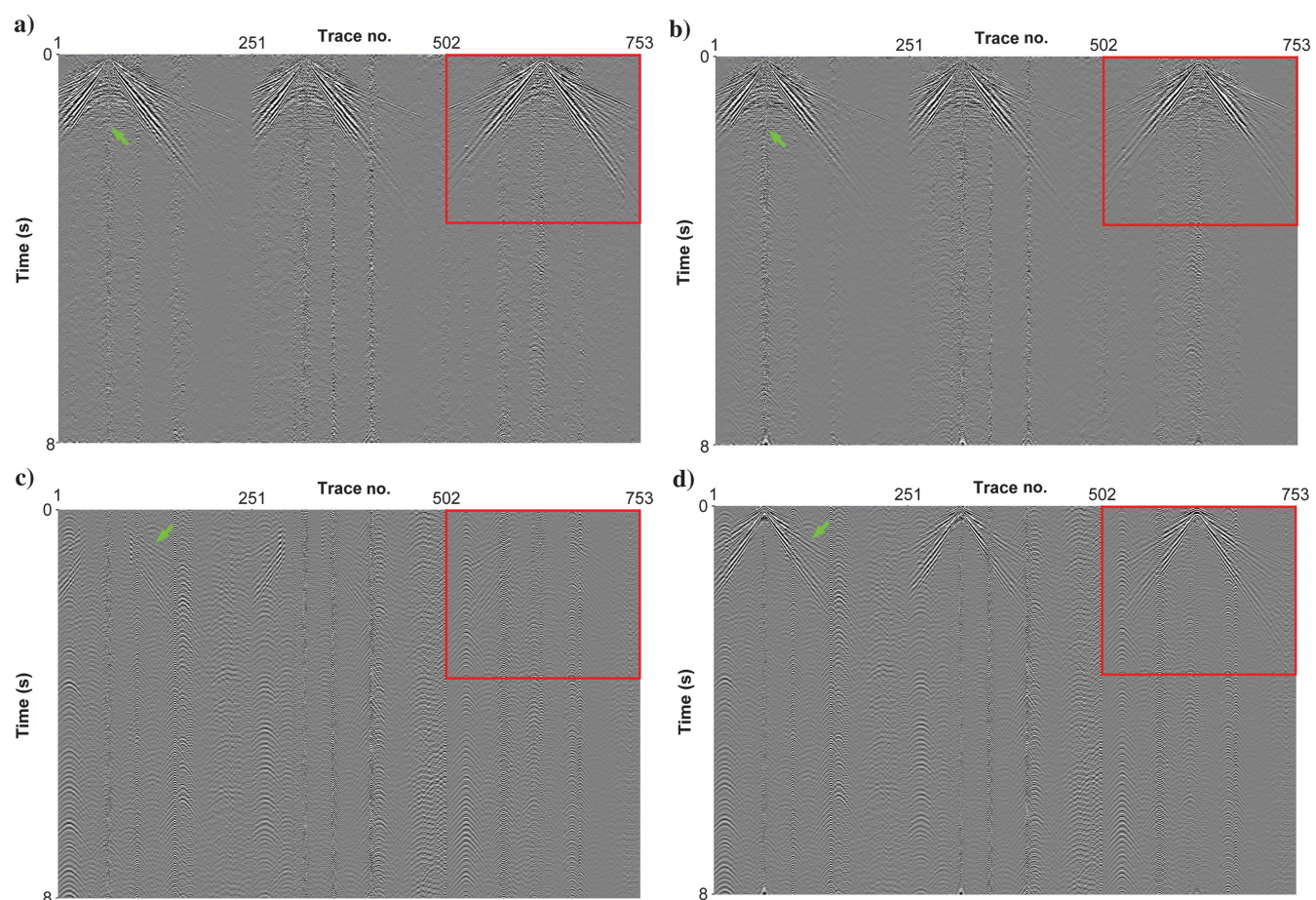


Figure 18. A comparison of separation results for three common-shot gathers shown in Figure 1 (some areas with obvious amplitude differences are marked with red boxes and green arrows). (a and c) Separated signals and WTN obtained by applying the proposed method and (b and d) separated signals and WTN obtained by applying the conventional method.

wavelet as an explosive point source. The first two layers in the model consist of a low-velocity layer with a thickness of 80 m and a velocity of 800 m/s, followed by a high-velocity layer with a thickness of 300 m and a velocity of 2500 m/s. The high-velocity layer is located beneath the low-velocity layer, and the remaining layers in the model are determined using the Gardner formula (Gardner et al., 1974).

To generate the contaminated data for our analysis, we take the first 100 traces and the time interval from 0 to 1.6 s from the WTN shown in Figure 5 and double its amplitude. Figure 14c shows the selected WTN with the doubled amplitude. Finally, the contaminated data shown in Figure 14d are the direct summation of the synthetic WTN shown in Figure 14c and the signals including the waves shown in Figure 14a and 14b. It has 100 traces and 800 samples per trace and a sample interval of 0.002 s.

The MCA with the TQWT ($Q = 1$) and the 1D DCT is the proposed method and the stationary biorthogonal-wavelet transform is the conventional method. Figure 15a and 15b shows separated signals and WTN from the proposed method, respectively. Figure 15c and 15d shows separated signals and WTN from the conventional method, respectively. Compared with the contaminated data shown in Figure 14d, Figure 15a and 15c exhibits clearer signals, whereas Figure 15b and 15d shows some leaked ground roll (the red arrows). However, Figure 15c exhibits noticeable leaked refractions (the red arrow) that are not present in Figure 15a at the same location. In addition, Figure 15d shows some leaked direct waves (the green arrow).

For further comparison, Figure 16a displays the 25th trace from the contaminated data shown in Figure 14d. Figure 16b displays three traces: the pure signal (a red curve) contained in the trace shown in Figure 16a, the separated signal from the proposed method (a black curve), and the separated signal from the conventional method (a green curve). Figure 16c also displays three traces: the pure WTN (a red curve) contained in the trace shown in Figure 16a, the separated WTN from the proposed method (a black curve), and the separated WTN from the conventional method (a green curve). In Figure 16b and 16c, the separated results from the proposed method (the black curves) are much closer to the original signal and WTN (the red curves) than the separated results from the conventional method (the green curves), particularly in the regions marked with the red arrows.

Figure 17a displays the time-frequency spectra of the contaminated trace shown in Figure 16a. Figure 17b and 17c shows the time-frequency spectra of the pure signal and WTN, respectively. Figure 17d and 17e shows the time-frequency spectra of the separated signal and WTN from the proposed method, respectively. Figure 17f and 17g shows the time-frequency spectra of the separated signal and WTN from the conventional method, respectively. Compared with Figure 17a, Figure 17d and 17f shows clearer signal energy, whereas Figure 17e and 17g shows clearer WTN energy. According to Figure 17b and 17c, Figure 17d shows more signal energy than Figure 17f, especially in the same locations around the red arrows, whereas Figure 17g exhibits some leaked signal energy around a red arrow.

These results indicate that the proposed method is effective in separating synthetic WTN and synthetic signals, including direct waves, refractions, and surface waves. It demonstrates better performance in preserving the original signal compared with the conventional method.

First field data application

In this section, three gathers shown in Figure 1 are taken to demonstrate the performance of the proposed method (MCA with the TQWT [$Q = 1$] and the 1D DCT) and the conventional method (stationary biorthogonal-wavelet transform) for the separation of signals and WTN. The separated signals and WTN from the proposed method are shown in Figure 18a and 18c, respectively, whereas the separated signals and WTN from the conventional method are shown in Figure 18b and 18d, respectively. We observe that Figure 18a exhibits clearer signals than Figure 18b, particularly in regions indicated by the green arrows. In addition, Figure 18d exhibits signal leakage around the location marked with a green arrow, whereas Figure 18c has almost invisible signal leakage around the same location marked with a green arrow.

To further analyze the results, the $f\text{-}k$ spectra of the first gather are shown in Figure 19a–19e, corresponding to the input data (Figure 1) and the separated results (Figure 18a–18d). The WTN is represented by the various frequency bands (the red arrows) in Figure 19a. More WTN energy is retained around the red arrows in Figure 19c than the same locations in Figure 19b. In addition, Figure 19d shows more separated WTN energy around the red arrows compared with

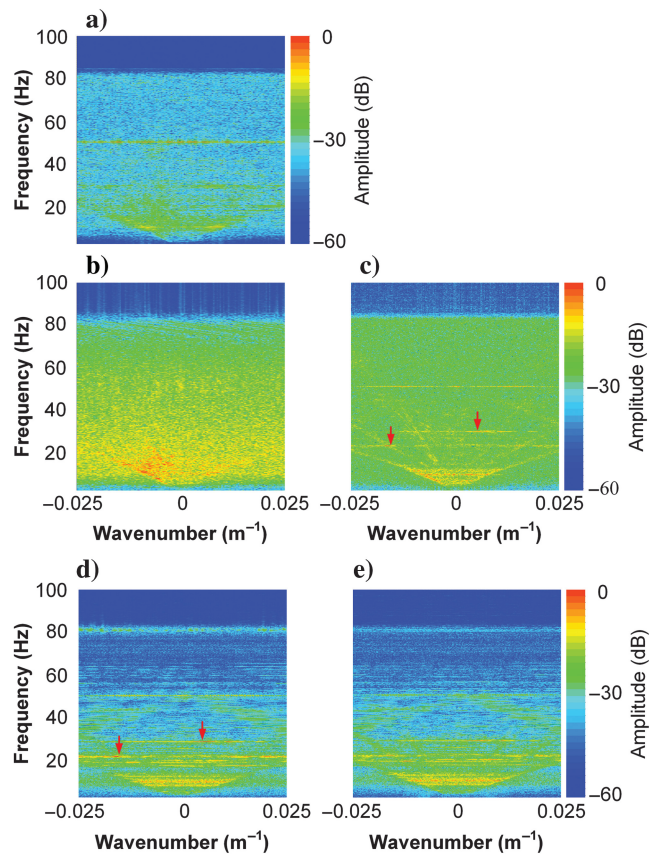


Figure 19. Comparison of the $f\text{-}k$ spectra of the original first gather in Figure 1 (some WTN energy is marked with the red arrows in [a, c, and d]). (a) The $f\text{-}k$ spectrum of the original first gather; (b and c) the $f\text{-}k$ spectra of the separated signals obtained by applying the proposed method and the conventional method to the first gather, respectively; and (d and e) the $f\text{-}k$ spectra of the separated WTN obtained by applying the proposed method and the conventional method to the first gather, respectively.

Figure 19e. For a detailed examination, Figure 20 provides a magnified view of the data within the red boxes in Figure 18, along with the original data from the same location in Figure 1. Figure 20a displays the input data, Figure 20b and 20c shows the separated results obtained by applying the proposed method, and Figure 20d and 20e shows the separated results obtained by applying the conventional method. Figure 20b exhibits clearer signals than Figure 20d, especially around the areas marked with red arrows. Figure 20e shows the leakage of signals, such as the reflection leakage marked with a red arrow, whereas Figure 20c shows no visible signals around the same area marked with a red arrow. Furthermore, Figure 21a shows the contaminated 78th trace in Figure 20a. Figure 21b and 21c shows the separated signals obtained by applying the proposed method and the conventional method to the contaminated 78th trace, respectively. Figure 21d and 21e shows separated WTN obtained by applying the proposed method and the conventional method to the

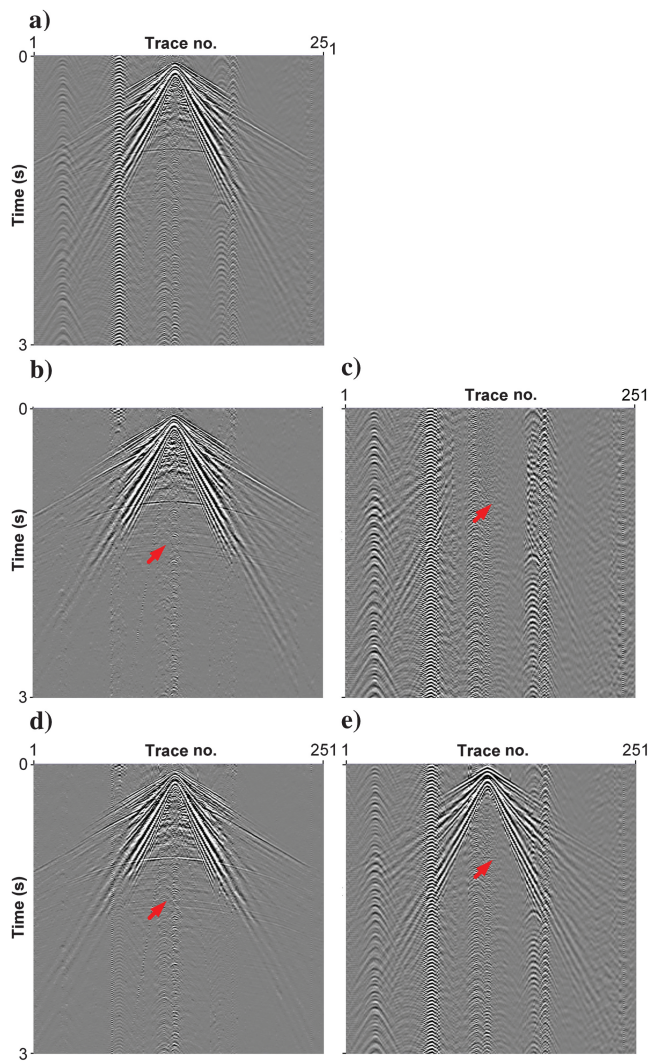


Figure 20. A magnified view of the separation results (the red boxes in Figure 18) (some areas with amplitude differences are marked with the red arrows in [b–e]). (a) The original third gather; (b and c) separated signals and WTN obtained by applying the proposed method, respectively; and (d and e) separated signals and WTN obtained by applying the conventional method, respectively.

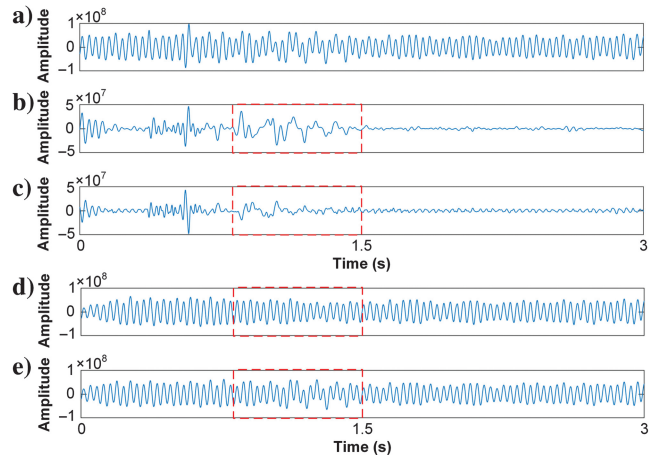


Figure 21. A comparison of the 78th trace's separation results for the third gather in Figure 1 (some areas with amplitude differences are marked with the dotted red boxes in [b–e]). (a) The original 78th trace between 0 and 3 s; (b and d) separated signals and WTN obtained by applying the proposed method, respectively; and (c and e) separated signals and WTN obtained by applying the conventional method, respectively.

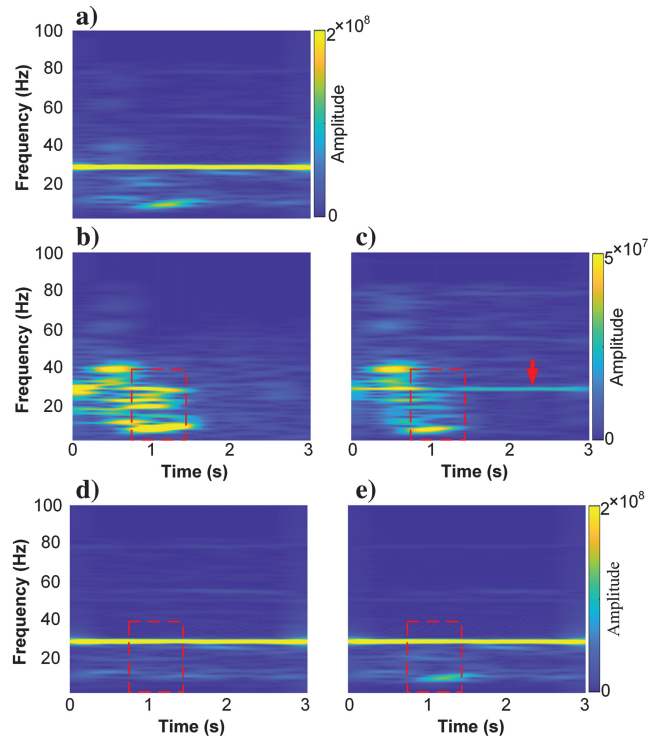


Figure 22. Time-frequency spectra of the 78th trace's time-frequency spectra for the third gather in Figure 1 (some areas with amplitude differences are marked with the dotted red boxes in [b–e] and the WTN energy in [c] is marked with a red arrow). (a) Time-frequency spectrum of the original 78th trace between 0 and 3 s; (b and c) time-frequency spectra of the separated signals obtained by applying the proposed method and the conventional method, respectively; and (d and e) time-frequency spectra of the separated WTN obtained by applying the proposed method and the conventional method, respectively.

contaminated 78th trace, respectively. The time-frequency spectra of Figure 21a–21e are shown in Figure 22a–22e, respectively. Comparing separated signals shown in Figure 21b and 21c with the contaminated 78th trace, both results from the proposed method and the conventional method show clearer signals. However, there are notable differences in the data bounded by the dashed red boxes in Figure 21b–21e, and their main energy is highlighted by the dashed red boxes in Figure 22b–22e. Figure 22c shows WTN energy (a red arrow). Figure 22b exhibits no visible WTN energy but more signal energy than Figure 22c, especially in the areas within the dashed boxes. Figure 22d shows no visible signal energy within the dashed red box, whereas Figure 22e shows the leakage of signal energy within the same area (a dashed red box). These results indicate that the proposed method is more effective in separating WTN from

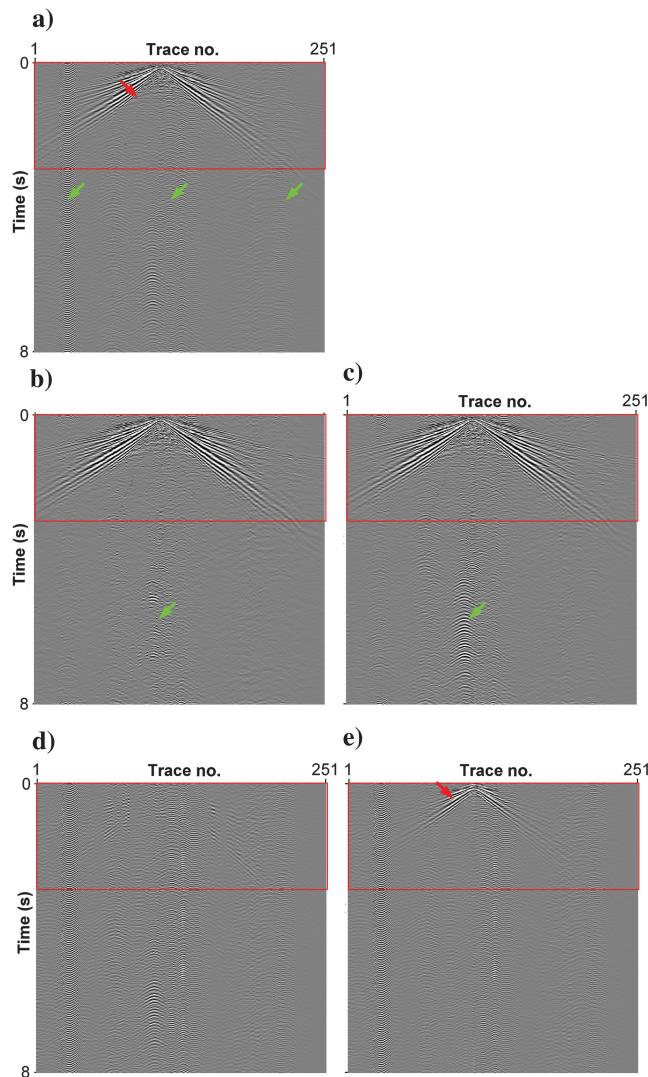


Figure 23. Second field data example (some areas contaminated with the WTN are marked with the green arrow and some signals are marked with the red arrows in [a and e]; the strongest signals are indicated by the red boxes). (a) A common-shot gather contaminated with some WTN having inconsistent energy in time; (b and c) separated signals from the proposed method and the conventional method, respectively; and (d and e) separated WTN from the proposed method and the conventional method, respectively.

common-shot gathers and better preserves signals compared with the conventional method.

Second field data application

A common-shot gather shown in Figure 23a is used as an example in this section. It is acquired in the same survey as the data used in the previous section (Figure 1), but they are acquired in different regions. In addition, the gather shown in Figure 23a is contaminated with some WTN (the second green arrow) whose energy obviously increases at approximately 4 s, but the gathers shown in Figure 1 mainly contain the WTN having consistent energy over time.

Figure 23b and 23c shows separated signals from the proposed method and the stationary biorthogonal-wavelet transform (the conventional method), respectively. Figure 23d and 23e shows separated WTN from the proposed method and the conventional method, respectively. Figure 23b and 23c shows clearer signals than Figure 23a. Figure 23b shows less WTN than Figure 23c, especially around the green arrows. There is signal leakage in Figure 23e (a red arrow), whereas there is no visible signal in the same location in Figure 23d. Figure 24a displays the f - k spectrum of the original data shown in Figure 23a. Figure 24b and 24c shows the f - k spectra of

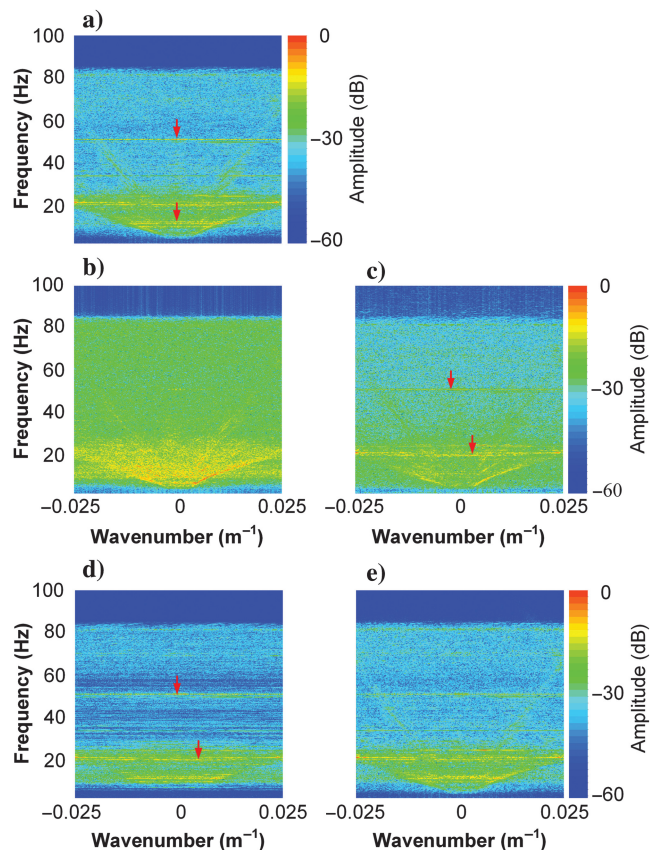


Figure 24. Comparison of the f - k spectra of the second field data example (some WTN energy is marked with the red arrows in [a, c, and d]). (a) The f - k spectrum of the second field example data; (b and c) the f - k spectra of the separated signals obtained by applying the proposed method and the conventional method, respectively; and (d and e) the f - k spectra of the separated WTN obtained by applying the proposed method and the conventional method, respectively.

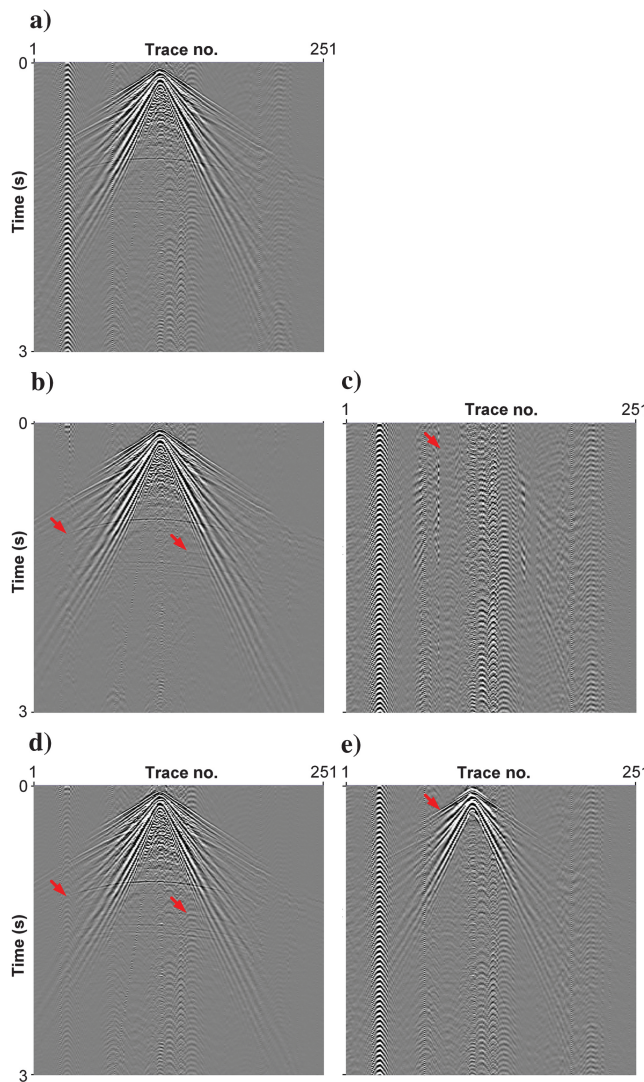


Figure 25. A magnified view of the separation results (the red boxes in Figure 23) (some areas with amplitude differences are marked with the red arrows in [b–e]). (a) Original data; (b and c) separated results obtained by applying the proposed method; and (d and e) separated results obtained by applying the conventional method.

separated signals from the proposed method and the conventional method, respectively. Figure 24d and 24e shows the f - k spectra of separated WTN from the proposed method and the conventional method, respectively. Figure 24b and 24c shows clearer signal energy than Figure 24a, but Figure 24c shows obvious WTN energy around the red arrows. Figure 24d and 24e shows the strongest WTN energy, but Figure 24d shows more WTN energy around the red arrows than Figure 24e. For further comparison, Figure 25 shows a magnified view of the data in the red boxes in Figure 23. Figure 25a shows the original data. Figure 25b and 25c shows separated signals and WTN from the proposed method, respectively. Figure 25d and 25e shows separated signals and WTN from the conventional method, respectively. The signals covered by WTN in Figure 25a are visible in the locations marked with the red arrows in Figure 25b, but they are still unclear in the locations marked with

the red arrows in Figure 25d. There is signal leakage in Figure 25e (a red arrow), whereas there are no visible signals at the same location in Figure 25c.

These results demonstrate that the proposed method can effectively separate the signals and WTN acquired in different locations in a survey.

CONCLUSION

This paper focuses on the formation and propagation mechanism of WTN in common-shot gathers and presents a rational WTN simulation model based on the mechanism of WTN. The proposed method for WTN separation is a trace-by-trace MCA-based method with constructed DCT and TQWT dictionaries, which avoids the need for spatial smoothing and the knowledge of wind turbine locations. The DCT and TQWT dictionaries are chosen to represent the periodic WTN and the low-oscillatory signals, satisfying the prerequisites of MCA. Moreover, we provide guidance on determining the appropriate Q -value for the TQWT dictionary. The ratio of the central frequency and bandwidth of the average amplitude spectrum of a signal-dominated data segment selected from given gathers can serve as an estimated Q -value for the TQWT dictionary. The synthetic and field data tests validate the effectiveness of the proposed method in separating WTN and preserving signals. The results demonstrate the effective separation of WTN and the preservation of signals.

In future work, we plan to explore the adaptation of high-dimensional dictionaries for modeling the morphological features of complex noises or signals. This involves selecting appropriate noise- or signal-dominated data segments and analyzing the formation and propagation mechanisms to extract significant morphological features. These tasks are important for further improving the understanding and separation of high-dimensional noises or signals in practical applications.

ACKNOWLEDGMENTS

This work is supported in part by the National Key Research and Development Program of China under Grant 2021YFA0716904 and in part by the National Natural Science Foundation of China under Grant 41974131 and Grant 41774135. Many thanks go to the assistant editor, S. Hestholm, and other anonymous reviewers for their insightful suggestions.

DATA AND MATERIALS AVAILABILITY

Data associated with this research are confidential and cannot be released.

REFERENCES

- Aharon, M., M. Elad, and A. M. Bruckstein, 2006, K-SVD: An algorithm for designing overcomplete dictionaries for sparse representation: *IEEE Transactions on Signal Processing*, **54**, 4311–4322, doi: [10.1109/TSP.2006.881199](https://doi.org/10.1109/TSP.2006.881199).
- Beresford-Smith, G., and R. N. Rango, 1988, Dispersive noise removal in t - x space: Application to arctic data: *Geophysics*, **53**, 346–358, doi: [10.1190/1.1442468](https://doi.org/10.1190/1.1442468).
- Brandon, T. L., M. P. Mintchev, and H. Tabler, 1999, Adaptive compensation of the mud pump noise in a measurement-while-drilling system: *SPE Journal*, **4**, 128–133, doi: [10.2118/56852-PA](https://doi.org/10.2118/56852-PA).

- Bruce, A. G., S. Sardy, and P. Tseng, 1998, Block coordinate relaxation methods for nonparametric target signal denoising: Proceedings of SPIE, **3391**, 75–86, doi: [10.1117/12.304915](https://doi.org/10.1117/12.304915).
- Chen, J., W. Chen, X. Wang, Y. Zhou, Z. Shi, and G. Zhang, 2018, DAS coupling noise suppression using wavelet and DCT dictionary based on sparse optimization: 88th Annual International Meeting, SEG, Expanded Abstracts, 4938–4942, doi: [10.1190/segam2018-2996038.1](https://doi.org/10.1190/segam2018-2996038.1).
- Chen, X., W. Chen, X. Wang, and W. Wang, 2017, Sparsity-optimized separation of body waves and ground-roll by constructing dictionaries using tunable Q-factor wavelet transforms with different Q-factors: Geophysical Journal International, **211**, 621–636, doi: [10.1093/gji/ggx332](https://doi.org/10.1093/gji/ggx332).
- Deighan, A. J., and D. R. Watts, 1997, Ground-roll suppression using the wavelet transform: Geophysics, **62**, 1896–1903, doi: [10.1190/1.1444290](https://doi.org/10.1190/1.1444290).
- Dong, W., Y. Xing, and T. Moan, 2012, Time domain modeling and analysis of dynamic gear contact force in a wind turbine gearbox with respect to fatigue assessment: Energies, **5**, 4350–4371, doi: [10.3390/en5114350](https://doi.org/10.3390/en5114350).
- Gao, S. W., B. Zhao, S. Y. Zhu, G. A. Luo, and Z. H. He, 2011, Identification and elimination of monofrequency interference in seismic data by an autocorrelation algorithm: Chinese Journal of Geophysics, **54**, 150–161, doi: [10.1002/cjg2.1596](https://doi.org/10.1002/cjg2.1596).
- Gardner, G. H. F., L. W. Gardner, and A. R. Gregory, 1974, Formation velocity and density — The diagnostic basics for stratigraphic traps: Geophysics, **39**, 770–780, doi: [10.1190/1.1440465](https://doi.org/10.1190/1.1440465).
- Guo, Y., S. Guo, K. Guo, and H. Zhou, 2021, Seismic data denoising under the morphological component analysis framework by dictionary learning: International Journal of Earth Sciences, **110**, 963–978, doi: [10.1007/s00531-021-02001-3](https://doi.org/10.1007/s00531-021-02001-3).
- Hoyer, P. O., 2004, Non-negative matrix factorization with sparseness constraints: Journal of Machine Learning Research, **5**, 1457–1469.
- Hu, Y., D. Liu, X. Wang, Z. Zhao, and W. Chen, 2022, Attenuation of the multiple reflection-refraction in 2-D common-shot gather via random-de-rangement-based FX Cadzow filter: IEEE Geoscience and Remote Sensing Letters, **19**, 1–5, doi: [10.1109/LGRS.2021.3051620](https://doi.org/10.1109/LGRS.2021.3051620).
- Kulesh, M., M. S. Diallo, M. Holschneider, K. Kurennaya, F. Krüger, M. Ohrnberger, and F. Scherbaum, 2007, Polarization analysis in the wavelet domain based on the adaptive covariance method: Geophysical Journal International, **170**, 667–678, doi: [10.1111/j.1365-246X.2007.03417.x](https://doi.org/10.1111/j.1365-246X.2007.03417.x).
- Lebedev, A. V., and I. A. Beresnev, 2004, Nonlinear distortion of signals radiated by vibroseis sources: Geophysics, **69**, 968–977, doi: [10.1190/1.1778240](https://doi.org/10.1190/1.1778240).
- Li, C., C. C. Mosher, and Y. Zhang, 2021, A direct noise attenuation approach in processing of land continuous records: The Leading Edge, **40**, 288–296, doi: [10.1190/tle40040288.1](https://doi.org/10.1190/tle40040288.1).
- Lin, D., L. Song, L. Lin, and C. Cheng, 2018, De-noising processing method in the process of drilling-oriented parameters transfer: Journal of Computational Methods in Sciences and Engineering, **19**, 289–298, doi: [10.3233/JCM-180864](https://doi.org/10.3233/JCM-180864).
- Liu, D., L. Gao, X. Wang, and W. Chen, 2021a, A dictionary learning method with atom splitting for seismic footprint suppression: Geophysics, **86**, no. 6, V509–V523, doi: [10.1190/geo2020-0681.1](https://doi.org/10.1190/geo2020-0681.1).
- Liu, D., X. Li, W. Wang, X. Wang, Z. Shi, and W. Chen, 2022a, Eliminating harmonic noise in vibroseis data through sparsity-promoted waveform modeling: Geophysics, **87**, no. 3, V183–V191, doi: [10.1190/geo2021-0448.1](https://doi.org/10.1190/geo2021-0448.1).
- Liu, D., M. D. Sacchi, X. Wang, and W. Chen, 2023, Unsupervised deep learning for ground roll and scattered noise attenuation: IEEE Transactions on Geoscience and Remote Sensing, 1–14, doi: [10.1109/TGRS.2023.3325324](https://doi.org/10.1109/TGRS.2023.3325324).
- Liu, D., H. Zhang, X. Wang, W. Chen, Z. Shi, and Z. Zhao, 2022b, Separation of seismic multiple reflection-refraction based on morphological component analysis with high-resolution linear Radon transform: Geophysics, **87**, no. 4, V367–V379, doi: [10.1190/geo2021-0468.1](https://doi.org/10.1190/geo2021-0468.1).
- Liu, N., F. Li, D. Wang, J. Gao, and Z. Xu, 2021b, Ground-roll separation and attenuation using curvelet-based multichannel variational mode decomposition: IEEE Transactions on Geoscience Remote Sensing, **60**, 1–14, doi: [10.1109/TGRS.2021.3054749](https://doi.org/10.1109/TGRS.2021.3054749).
- Liu, Y., X. Chen, R. K. Ward, and Z. J. Wang, 2019, Medical image fusion via convolutional sparsity based morphological component analysis: IEEE Signal Processing Letters, **26**, 485–489, doi: [10.1109/LSP.2019.2895749](https://doi.org/10.1109/LSP.2019.2895749).
- Liu, Z., Y. Chen, and J. Ma, 2018, Ground roll attenuation by synchro-squeezed curvelet transform: Journal of Applied Geophysics, **151**, 246–262, doi: [10.1016/j.jappgeo.2018.02.016](https://doi.org/10.1016/j.jappgeo.2018.02.016).
- Lyons, J. P., M. C. Robinson, P. Veers, and R. W. Thresher, 2008, Wind turbine technology — The path to 20% US electrical energy: IEEE Power & Energy Society General Meeting-Conversation & Delivery of Electrical Energy in the Century.
- Namuq, M. A., and M. Reich, 2010, Laboratory experiments on pressure wave propagation in drill strings (mud pulse telemetry): Oil Gas European Magazine, **36**, 119–125.
- Namuq, M. A., M. Reich, and S. Bernstein, 2013, Continuous wavelet transformation: A novel approach for better detection of mud pulses: Journal of Petroleum Science & Engineering, **110**, 232–242, doi: [10.1016/j.petrol.2013.08.052](https://doi.org/10.1016/j.petrol.2013.08.052).
- Olshausen, B. A., and D. J. Field, 1996, Emergence of simple-cell receptive field properties by learning a sparse code for natural images: Nature, **381**, 607–609, doi: [10.1038/381607a0](https://doi.org/10.1038/381607a0).
- Oyague, F., 2009, GRC drive train round Robin GRC 750/48.2 loading document (IEC 61400-1 Class IIB): National Renewable Energy Laboratory.
- Qu, F., Q. Jiang, G. Jin, Y. Wei, and Z. Wang, 2021, Noise cancellation for continuous wave mud pulse telemetry based on empirical mode decomposition and particle swarm optimization: Journal of Petroleum Science and Engineering, **200**, 108308, doi: [10.1016/j.petrol.2020.108308](https://doi.org/10.1016/j.petrol.2020.108308).
- Rubinstein, R., A. M. Bruckstein, and M. Elad, 2010, Dictionaries for sparse representation modeling: Proceedings of the IEEE, **98**, 1045–1057, doi: [10.1109/JPROC.2010.2040551](https://doi.org/10.1109/JPROC.2010.2040551).
- Rubinstein, R., T. Peleg, and M. Elad, 2013, Analysis K-SVD: A dictionary-learning algorithm for the analysis sparse model: IEEE Transactions on Signal Processing, **61**, 661–677, doi: [10.1109/TSP.2012.2226445](https://doi.org/10.1109/TSP.2012.2226445).
- Selesnick, I. W., 2011a, TQWT toolbox guide: Electrical and Computer Engineering, Polytechnic Institute of New York University, <http://eeeweb.poly.edu/iselesni/TQWT/index.html>, accessed 6 October 2011.
- Selesnick, I. W., 2011b, Wavelet transform with tunable Q-factor: IEEE Transactions on Signal Processing, **59**, 3560–3575, doi: [10.1109/TSP.2011.2143711](https://doi.org/10.1109/TSP.2011.2143711).
- Starck, J. L., M. Elad, and D. L. Donoho, 2004, Redundant multiscale transforms and their application for morphological component analysis: Advances in Imaging and Electron Physics, **132**, 287–348, doi: [10.1016/S1076-5670\(04\)32006-9](https://doi.org/10.1016/S1076-5670(04)32006-9).
- Tao, Y., S. Cao, Y. Ma, and M. Ma, 2020, Second-order adaptive synchro-squeezing S transform and its application in seismic ground roll attenuation: IEEE Geoscience Remote Sensing Letters, **17**, 1308–1312, doi: [10.1109/LGRS.2019.2946368](https://doi.org/10.1109/LGRS.2019.2946368).
- Walling, R. A., E. Gursoy, and B. English, 2011, Current contributions from Type 3 and Type 4 wind turbine generators during faults: IEEE Power and Energy Society General Meeting.
- Wang, W., W. Chen, J. Lei, and J. Gao, 2010, Ground roll separation by sparsity and morphological diversity promotion: 80th Annual International Meeting, SEG, Expanded Abstracts, 3705–3710, doi: [10.1190/1.3513621](https://doi.org/10.1190/1.3513621).
- Wang, X., C. Yang, X. Li, W. Chen, and H. Zhao, 2017, An iterative method for well-pump noise attenuation in the time-frequency domain: 87th Annual International Meeting, SEG, Expanded Abstracts, 4970–4974, doi: [10.1190/segam2017-17746045.1](https://doi.org/10.1190/segam2017-17746045.1).
- Yarham, C., U. Boeniger, F. Herrmann, and U. B. Columbia, 2006, Curvelet-based ground roll removal: 76th Annual International Meeting, SEG, Expanded Abstracts, 2777–2782, doi: [10.1190/1.2370101](https://doi.org/10.1190/1.2370101).
- Yu, Z., and P. Garossino, 2005, High-energy noise attenuation of seismic data in the wavelet-transform domain: Integrated Computer Aided Engineering, **12**, 57–67, doi: [10.3233/ICA-2005-12105](https://doi.org/10.3233/ICA-2005-12105).

Biographies and photographs of the authors are not available.